TURBO-16-1218

# Parasitic loss due to leading edge instrumentation on a low pressure turbine blade.

**Henry C.-H. Ng***

Whittle Laboratory

University of Cambridge

United Kingdom

Email: hchn2@cam.ac.uk

**John D. Coull**

Whittle Laboratory

University of Cambridge

United Kingdom

Email: jdc38@cam.ac.uk

**ABSTRACT**

During the testing of development engines and components, intrusive instrumentation such as Kiel head Pitot probes and shrouded thermocouples are used to evaluate gas properties and performance. The size of these instruments can be significant relative to the blades and their impact on aerodynamic efficiency must be considered when analysing the test data. This paper reports on such parasitic losses for instruments mounted on the leading edge of a stator in a low pressure turbine, with particular emphasis on understanding the impact of probe geometry on the induced loss.

The instrumentation and turbine blades were modelled in a low Mach number cascade facility with an upstream turbulence grid. The cascade was designed so that leading edge probes were interchangeable in-situ, allowing for rapid testing of differing probe geometries. RANS calculations were performed to complement the experiments and improve understanding of the flow behaviour.

A horseshoe vortex-like system forms where the probe body joins the blade leading edge, generating pairs of streamwise vortices which convect over the blade pressure and suction surfaces. These vortices promote mixing

between the freestream and boundary layer fluid, and promote the transition of the boundary layer from laminar to turbulent flow.

Tests with realistic probe geometries demonstrated that the design of the shroud bleed system can impact losses and a study using idealised cylinders was performed to isolate the impact of probe diameter, aspect ratio and incidence. Beyond a probe aspect ratio of two; parasitic loss was found to scale with probe frontal area.

## 1 INTRODUCTION

In order to accurately measure the performance and operating characteristics of a gas turbine engine and its components, it is necessary to know the variation of total pressure and temperature through the machine. In practice this is achieved by mounting pressure and temperature probes at various axial and radial positions within a development engine, typically by means of instrumentation rakes or by mounting instrumentation to the leading edge of existing engine hardware such as stator vanes. Instruments with Kiel [1] shrouds are most commonly deployed as the presence of the shroud provides several advantages. For total pressure measurements the shroud desensitises the probe to incidence angle, improving accuracy in the highly swirling flows typical of turbomachines. For total temperature measurement, a shroud is required to slow the gas flow over the sensing element in order to measure the stagnation temperature. For an ideal temperature sensor, the gas would be slowed adiabatically and a true measurement of stagnation temperature would be acquired. In practice, however, there are complex heat transfer mechanisms within the sensors and probes themselves and thus the measured temperature, $T_m$, will be less than the true stagnation temperature, $T_t$. This difference is accounted for with a temperature recovery factor defined as;

$$R_f = \frac{T_m - T_s}{T_t - T_s}, \tag{1}$$

where $T_s$ is the static temperature. The priority of the probe designer is to maximise this value in order to obtain accurate temperature measurements, which generally necessitates relatively large shrouds to maximise thermal isolation.

The deployed probes will introduce additional aerodynamic losses into the engine, which must be accounted for when calculating the equivalent “clean” engine performance. An accurate understanding of the aerodynamic effects and loss is therefore needed to minimize errors. Whilst investigations into shroud design and probe performance for various angles of attack, Reynolds and Mach numbers have been carried out [2, 3], little has been done to assess the aerodynamic impact of these pressure and temperature Kiel probes on the flow through a turbomachine. One exception is the work of Lepicovsky [4] who studied the rotor exit flow field of a compressor stage. A total pressure Kiel probe was deployed on a stem in a single rotor passage, being mounted from the hub and located close to the leading edge at the midspan radius. The pressure Kiel and stem had a geometric blockage of approximately 3.5% based on the probe projected area. Phase locked ensemble average

pressure and velocity fields were obtained by traversing pressure probes and a split-fibre probe over an area at the rotor exit plane downstream of the pressure Kiel. Lepicovsky reported significantly reduced total pressure in the wake of the Kiel probe, as well as a large amount of flow blockage in the blade passage, where the flow separated from the suction side of the compressor blade for over 20% of the blade surface. Lepicovsky further reported redistribution in the vicinity of the pressure Kiel. The instrumented rotor passage experienced an overall axial velocity deficit of 4% relative to clean sectors, which was counterbalanced by a slight increase in axial velocity for adjacent passages. Furthermore, the flow within the instrumented passage itself redistributed towards the casing in response to the blockage.

To the authors' knowledge, there exists no published study of the aerodynamic impact of leading edge probes and therefore it is unclear how to account for the above losses. To address this deficiency, this paper explores the impact of leading edge pressure and temperature Kiels mounted on a Nozzle Guide Vane (NGV) that is representative of a Low Pressure Turbine (LPT) in a modern civil aeroengine. Emphasis is placed on understanding the fundamental flow features produced by the presence of such probes and the aerodynamic impact of probe geometric parameters on profile losses. As detailed in section 2, experiments are conducted in a low speed linear cascade and are complemented by steady RANS calculations of matching geometries. The impact of realistic Kiels is examined in section 3, followed by a study of the importance of shroud detailed design in section 4. A parametric study of probe diameter and length is reported in section 5, followed finally by conclusions in section 6.

## 2 METHODS

### 2.1 Experiments

Experiments were carried out in a low Mach number ($M_2 < 0.1$) linear cascade with an upstream turbulence grid and moving bar wake generator (figure 1); the wake generator was not used in this study. This rig is based on that used by several authors (e.g. Steiger and Hodson [5]) but re-bladed with a low turning NGV. The key design parameters are given in table 1. A comparison of the measured surface static pressure coefficient normalised by the trailing edge value ($C_{p_{(TE)}}$) and Mises [6, 7] design intent are plotted in figure 2. The Mises calculation has been performed with suction side transition specified at $S/S_0 = 0.6$ marked on figure 2 as point 'A'. The measured distribution indicates that at this Reynolds number ($Re = 330000$ based on exit velocity and true chord) there is a separation bubble between $0.8 < S/S_0 < 0.9$ (between 'B' and 'C' in figure 2). The static pressure distribution will be discussed in more detail in section 5.1.

The cascade is comprised of 5 blades and 4 passages. Measurements are performed on the central vane to which leading edge probes may be mounted. The central vane was constructed using stereolithography (SLA) which allowed for integrated pressure lines and surface static pressure tappings with 28 located on the suction side and 16 on the pressure side. Two parallel lines of pressure tappings were used, one located at blade midspan $z/h = 0.500$, directly in the shadow of a leading edge (LE) probe, and at $z/h = 0.583$ which is in-between two adjacent LE probes. Surface static pressure distributions were measured at each spanwise location by taping over the pressure tappings at the other spanwise location; the tape was removed

for all loss measurements.

The instrumented blade was designed with LE sockets which allowed probes to be readily interchanged. A total of five LE probes were fitted to the blade at equi-spaced locations of $z/h = 0.167$, 0.333, 0.500, 0.667 and 0.833. The probes were designed to incorporate an o-ring to aid in alignment and sealing of the probe and blade LE junction. The LE probe models were 3D printed in-house and all probe diameters and lengths quoted in this paper refer only to the exposed part of the probe forward of the blade LE.

A turbulence grid was installed an axial distance of 0.64m upstream of the LE of the central vane to give a freestream turbulence intensity level of $Tu \approx 4\%$ and length-scale of $L_x = 0.012$m according to the correlations of Roach [8].

Flow measurements were conducted using a 5 hole pressure probe of conical design, with a total head diameter of $D_{5HP} = 2.2$mm. The probe was calibrated in a free jet at 5 different probe Reynolds numbers, $2500 < Re_{5HP} = D_{5HP}U_\infty/\nu < 10000$, for pitch and yaw angles of up to $\pm 30^\circ$, in $2^\circ$ increments. The probe is traversed in a spanwise-pitchwise plane at an axial distance of $0.5C_x$ downstream of the blade trailing edge and covers 73% of the cascade span beginning at a distance of 2% of span from the endwall. The measurement grid has 37 points in the pitchwise direction and 67 points in the spanwise direction, with clustering near both the blade wakes and the LE probe wakes (see symbols on figures 7 to 9). Pressures were recorded using a *DSA 3127/16Px* pressure transducer and the calibration was applied using a two-dimensional interpolation to yield flow angles, velocity and total and static pressures. The total pressure loss coefficient used throughout this paper is defined as;

$$Y_p = \frac{P_{01} - P_{02}}{P_{01} - P_2}, \tag{2}$$

where $P_{01}$ is the mass averaged inlet total pressure and $P_{02}$ and $P_2$ are the exit total pressure and area averaged exit static pressure, respectively: Mass averaged values of $Y_p$ are obtained by integrating over the middle 50% of blade span which corresponds to 3 whole LE instrument pitches. This area was chosen as it encompasses the nominally two dimensional region of the flow which allows one to assess the impact of parasitic losses on profile loss which tends to dominate in LP turbines. The experimental uncertainty in mass averaged $Y_p$ is approximately $\pm 0.001$.

Periodicity was achieved by incrementally adjusting the angle of the tailboards mounted to the trailing edges of the top and bottom blade (figure 1). Figure 3 plots yaw angle and $Y_p$ measured at cascade midspan for approximately 3 blade passages. It can be seen that the flow angle and loss coefficient remain nominally periodic in the pitchwise direction, with only small deviations.

In this paper, unless otherwise stated, the flow Reynolds number is defined using the blade true chord and mass-averaged

exit velocity. Steady flow measurements were made at a Reynolds number of $Re = 330000$ with the moving bars removed from the wake generator so that there was no obstruction at the cascade inlet.

### 2.2 CFD

Unstructured meshes were generated for a single cascade passage using BoxerMesh v3.6.2., which uses an Octree approach to generate a hex-dominant grid with viscous surface layers. Unstructured meshing has several advantages over structured meshing for the current application, allowing mesh points to be concentrated in regions of significant flow gradients.

Steady RANS calculations of a single cascade passage were performed using the Rolls-Royce in-house solver HYDRA; further details of this code are given by Moinier and Giles [9]. The spatial discretization is based on an upwind edge-based finite volume scheme and is second-order accurate. Calculations were performed using the two-equation Shear-Stress Transport (SST) turbulence model. Boundary layers were modeled as fully turbulent; while significant regions of laminar flow are present in the experiments, it will be shown that the calculations nonetheless achieve reasonable agreement with the flow structures and additional parasitic losses introduced.

A mesh sensitivity study was conducted on the uninstrumented vane by specifying fixed levels of local refinement and incrementally increasing the global grid refinement. At all wall surfaces, 12 viscous layer cells are prescribed. Viscous layer cell height growth follows a power law distribution where the height of the first off wall cell is chosen to give a maximum $y^+$ of unity. In the wake region downstream of the vane, volume refinement was specified to better capture the large flow gradients. Figure 4 shows the sensitivity of $Y_p$ to global mesh density, obtained using the final mesh refinement template. The case with $\approx 17$ million cells was selected since further refinements caused changes in the loss coefficient of less than 0.0003, which was deemed to be acceptably grid independent. A subsequent study of local refinement levels for an instrumented case is also shown in figure 4 and the final mesh is shown in figure 5.

## 3 IMPACT OF REALISTIC PROBES

This section presents the results from a typical Kiel-head total pressure probe and a Kiel-head temperature probe, sketches of which are depicted in figure 6. The shrouds have bleed holes which are typically orientated normal to the blade span.

Figure 7 presents contours of yaw angle, pitch angle and total pressure loss coefficient for the uninstrumented vane, measured using a calibrated 5-hole pressure probe. The area traverse in the exit plane of the cascade covers one blade pitch and over 70% of the blade span, and the black triangles lining the edge of the contour plots indicate the spacings of the measurement grid. It can be seen in figure 7c that the uninstrumented vane has a nominally two-dimensional wake between

$\pm$35% of the cascade span. Towards the endwalls a typical pattern of secondary flow is evident, characterised by regions of underturning (A) and overturning (B), with an intense loss core at around 5% of span from the endwall (C).

Figures 8 and 9 display equivalent plots for measurements where leading edge pressure Kiels and temperature Kiels have been mounted, respectively. In general the two sets of instrumentation give similar effects but they are more pronounced for the larger temperature probe. It can be seen that the presence of LE probes produces regions of local overturning on the pressure side which increases with probe size (D). Along the blade span, the yaw angle alternates between over- and underturning on the pressure side. The pitch angle also alternates between positive and negative values. This "checkerboard" pattern in the flow angles is indicative of large scale streamwise vortex pairs. For the instrumented blades, the contours of $Y_p$ show additional loss cores (E) in the wake directly behind each of the LE probes. The loss cores are larger for the temperature probes than for the pressure probes. For the temperature Kiels (figure 9), there are secondary loss cores or plumes that expand tangentially into the freestream on both the pressure side (F) and suction side (G). These plumes are weaker than both the endwall loss cores and the primary loss cores of the LE probes.

The surface flow patterns have been examined using oil and dye flow visualisation of the blade surface which indicates vortex lift-off lines on the blade surface behind the LE probes. It is believed that these lift-off lines are formed by the legs of a horseshoe vortex-like (HSV) system. Typical images are shown in figure 10 for the temperature Kiel, where the lift-off lines associated with the legs of the HSV system can be seen. HSV systems form when a wall bounded shear flow encounters an obstruction that is perpendicular to the wall and orthogonal to the mean flow direction. The fundamental example is a circular cylinder mounted vertically on a flat wall [10–12]: the boundary layer on the flat wall encounters a strong adverse pressure gradient due to the potential field of the cylinder, separates and rolls up into a vortex system that wraps around the cylinder, forming a horseshoe shape, as it is advected downstream by the mean flow.

A similar phenomenon occurs when the boundary layer on the cylindrical surface of the probe encounters the aerofoil LE, forming a pair of horseshoe vortices either side of the probe. An interrogation of the CFD results allows one to view the flow structures forming at the LE probe and blade LE junction. The vortex identification method of Hunt et. al. [13] has been used for vortex identification and isosurfaces of Q-criterion, colored by the sign of the axial vorticity to indicate rotational direction, are displayed in figures 11a and 11d. These show a LE temperature Kiel from the suction side and pressure side, respectively. The following features are evident;

1. A vortex 'ring' can be seen forming on the LE probe shroud (A). As this ring of vorticity encounters the LE probe and blade LE junction (B), a pair of horseshoe vortices forms and wraps around the blade LE. The legs of the horseshoe vortex advect downstream on both the suction (C) and pressure sides (C'). These vortex pairs are believed to be responsible for the loss plumes (F and G in figure 9) since they act to eject low momentum boundary layer fluid away from the blade surfaces.

2. A second flow feature is also evident in the CFD results. Flow is ejected from the shroud bleed holes in a similar manner to a jet in crossflow. It is known that crossflow jets interact with the mean flow and generate kidney-like vortices [14–17] and this phenomena is commonly observed in turbomachinery in film cooling applications [18]. Figures 11a and 11d show pairs of kidney vortices (D) and (D') forming on the LE probe body in the presence of the shroud bleed holes. The suction side kidney vortices lift-off from the surface (D), an effect which can be ascribed to the lower static pressure and hence larger blowing ratio on this side. However, it will be shown in section 4.1 that these kidney vortices make only a small contribution to the overall parasitic loss.

Displayed in figures 11b and 11e are the corresponding isosurface of negative axial velocity which approximately identify regions of flow separation associated with the vortex structures. These isosurfaces of negative axial velocity reveal that flow separates from the leading edge of the probe in a similar manner to a bluff body. The separated region is asymmetric due to the static field of the blade, being slightly larger on the pressure side than the suction side. The flow over the outer surface of the probe tends to be swept upwards towards the suction side in the direction of the passage pressure gradient. This effect is apparent in the surface streamlines of the LE probe shown in figures 11c and 11f. The observations from CFD corroborate those from flow visualisation (figure 10), revealing the HSV system at the probe-blade junction and more detailed flow structures.

## 4 IMPACT OF SHROUD DETAILS ON LOSS

As the CFD results indicate, there is significant detail in the flow inside the shroud and ejection from the bleed holes, but it is not immediately clear whether these effects have a significant impact in the parasitic losses. This section therefore details an experimental investigation of the sensitivity of loss to the detailed probe design.

### 4.1 Sensitivity to shroud bleed hole orientation

A study was conducted to examine the effect of the presence of the shroud bleed holes (SBH), as well as the direction of the jet exiting the shroud relative to the standard installation. Five tests cases were carried out on the temperature Kiel;

1. shroud bleed holes at design,
2. shroud bleed holes rotated 45 degrees,
3. shroud bleed holes rotated 90 degrees,
4. shroud bleed holes covered and
5. a solid cylinder.

In the default case, the shroud bleed holes are orientated such that the mass flow exiting the LE probe is orthogonal to the blade LE as shown in figures 10 and 11. Contours of the measured total pressure loss coefficient for each configuration are plotted in figure 12.

It is clear from figure 12 that the presence and orientation of the shroud bleed holes has an influence on the flow field and that there is a redistribution of the measured losses. Given the presence of the kidney vortices generated by the shroud bleed holes (D in figure 11), it can be postulated that these sensitivities are partly governed by changes in the blowing ratio, trajectory of the ejected jet and mixing loss as the shroud is re-oriented. For case (2) where the shroud bleed holes are rotated 45 degrees, the additional loss cores migrate down the blade span on the pressure side (A) and up the blade span on the suction side (B) which is consistent with the movement of the shroud bleed holes. For case (3) where shroud bleed holes are at 90 degrees, the additional loss "plumes" (C) and (D) are significantly reduced in magnitude. The bleed holes exit to a higher static pressure in this orientation and therefore one would expect the flow rates to be significantly reduced. Case (4), where the shroud bleed holes are covered, behaves in a very similar fashion to case (3) and in fact their total pressure loss coefficients are nearly identical (see table 2). Finally, in case (5) where the temperature Kiel has been replaced by a solid cylinder, the behaviour is very similar to that of case (4), except for the LE probe nearest the endwall (E). The difference observed near the endwall is believed to be caused by an interaction of the secondary flow structures and the flow around the probe, which appears to be highly sensitive to the detailed geometry. Further analysis of these interactions is underway, but falls outside the scope of this paper which focuses on midspan flows.

While the orientation of the shroud bleed holes makes a difference to the flow field, the total pressure loss coefficient mass averaged over the central $\pm 25\%$ of span is similar for most cases. The mass averaged total pressure loss coefficients are presented in table 2 together with the difference in loss with the clean blade and the temperature Kiel. The difference between a temperature Kiel and a cylinder is small, with a change of less than 2% of the total loss, suggesting that the loss owing to the shroud bleed holes and the associated kidney vortices is small. Comparing the values in table 2, one can see that the parasitic loss due to the presence of a temperature Kiel is an order of magnitude larger than any change in losses due to the presence and orientation of shroud bleed holes. The only exception appears to be the $45^\circ$ case. For simplicity, the remainder of this paper therefore concentrates on the idealised solid cylinder models.

### 4.2 Sensitivity to probe incidence

Another parameter investigated in the study of shroud details was the impact of LE probe incidence relative to the blade inflow angle. In order to change the LE probe incidence, cylindrical probes were printed with "dog legs". These LE probes were of equivalent diameter ($D_{probe}/C_x = 0.10$) and length ($L_{probe}/C_x = 0.18$) to that of the temperature Kiel. Incidence relative to design was varied from $-10$ to $+10$ degrees in 5 degree increments. A schematic of the LE probe and blade LE junction displaying probes at both positive and negative yaw and pitch angles is shown in figure 13. Measurements at negative pitch angles were not tested given the symmetry of the cascade.

Figure 14 displays contours of measured total pressure loss for LE probe yaw angles of $-10$ degrees to $+10$ degrees. In general, yaw has a large effect on the relative strengths of the loss plumes observed (eg. figure 9: F and G). When the LE probe yaw angle is negative, the additional loss cores or plumes on the pressure side (A and C) increases in size with

yaw angle, relative to when the LE probes are at zero incidence (E). When the LE probe yaw angle is $-5$ degrees, the loss plume on the suction side is still present (D), but at a yaw angle of $-10$ degrees, this is no longer visible (B). Further, at $-10$ degrees yaw, the loss cores in the wake due to the LE probe (B) have migrated towards each other. The reason for this is not clear, but it suggests that this case is very sensitive to any small misalignment of the probe. When the yaw angle is positive, the loss plumes on the suction side (G and H) increase with increasing yaw and both are larger than when the the yaw angle is zero (F). Conversely, on the pressure side the loss plumes reduce in magnitude with increasing positive yaw.

Figure 15 displays the measured total pressure loss for LE probes mounted at pitch angles of $+5$ and $+10$ degrees. The shape of the loss cores when LE probes have non-zero pitch angles (C) and (D), become increasingly asymmetric. In particular, the main loss cores labeled (C) and (D) are skewed in the direction of the LE probe pitch angle, as are the loss plumes. Further, it can be seen that the strength of the loss cores (C) and (D) increases with increasing pitch. This pitch variation is much more pronounced than the yaw sensitivity (figure 14: B, D, F, G, H).

Figure 16 displays the total pressure loss coefficient measured at cascade exit as a function of the probe incidence with yaw angles plotted in circles and pitch angles plotted in squares. It appears that for off-design yaw angles of up to $\pm 10^\circ$ there is a reduction in loss regardless of whether the LE probes have a positive or negative incidence. However, this does not hold true for the pitch angle variation, where losses increased by 30% at 10 degree incidence. Gracey [3] reports that pressure Kiels with well designed shrouds were capable of measuring total pressure to within 1% of the impact pressure for incidence angles of up to $28^\circ$ at $M \approx 0.26$. The values of LE probe incidence tested in this study are well within these limits. The results underline the sensitivity of parasitic losses to incidence, which must be carefully considered when accounting for loss.

## 5 IMPACT OF PROBE SIZE

In order to generalise the results it is desirable to understand the impact of the overall probe size on the induced losses. To this end a study of cylinders has been performed to independently examine the effect of probe diameter and length. For the following comparisons of experiments and CFD, the CFD has been normalised to the calculated clean profile, which has a different loss than the experimental baseline (1.53% versus 1.66%) because of modeling the boundary layers as fully turbulent.

### 5.1 Diameter

Given the flow separation noted in figure 11b and 11e one may expect the probes to behave as simple bluff bodies, such that the parasitic losses are proportional to frontal area. The data lend some support to this hypothesis. Figure 17 demonstrates the increase in total pressure loss coefficient, $Y_p$, with LE probe diameter, $D_{probe}$, for cylinders and realistic probe geometries. Figure 18 shows the equivalent plot of $Y_p$ against probe frontal area ($D^2_{probe}$); to a first order, $Y_p$ scales linearly with the probe frontal area. This trend is consistent in both the experimental and CFD results. For reference, the

green dashed line in figure 18 represents the loss predicted by a drag co-efficient of $C_d = 0.85$ at the upstream dynamic head which is the value reported by Hoerner [19] for high aspect ratio cylinders in axial flow. The close agreement in trends lends further support to the notion that parasitic loss induced by LE probes is proportional to probe frontal area.

Whilst the general trends between experiment and CFD are in agreement, some interesting features are also observed: for LE probes of small diameter ($D_{probe}/C_x = 0.03$), mass averaged $Y_p$ measured in the experiments decreases relative to the uninstrumented vane. It will be shown that for the experiments, a small LE probe causes a decrease in total pressure loss by promoting early transition on the blade surface at this operating condition. A similar reduction can be achieved by placing a trip on the clean blade. This reduction in loss is not captured in the fully-turbulent CFD calculation.

The CFD results in figure 17 also show a small abrupt increase in $Y_p$ when moving from LE probe sizes $D_{probe}/C_x = 0.02$ to 0.03. It is hypothesized that the presence of the blade LE may prevent significant flow separation for such small probes ($D_{probe}/C_x < 0.02$), thus reducing the form drag. Further work would be needed to investigate this phenomenon in detail, but the effect is small.

Figure 19 shows the measured blade static pressure coefficient profiles, normalised by trailing edge value, for an uninstrumented vane and with cylinders of $D_{probe}/C_x = 0.03$ mounted on the leading edge. This case corresponds to the minimum loss observed in figure 17. The Mises distribution is plotted alongside for comparison, with a specified transition location of $S/S_0 = 0.6$ (A). Comparing the pressure profile between the Mises distribution and the uninstrumented vane; there is a clear plateau on the measured suction side distribution for $0.8 < S/S_0 < 0.9$, (B) and (C), indicating the presence of a separation bubble. With the LE probe of $D_{probe}/C_x = 0.03$ the separation bubble is fully suppressed directly behind the probe ($z/h = 0.5$), and partially suppressed between probes ($z/h = 0.583$). The suppression of the separation bubble is also apparent in the flow visualisation images presented in figure 20 which show the blade suction surface as viewed from trailing edge to leading edge. The top image is of the uninstrumented vane and there clearly exists a region of separation near the trailing edge between lines (B) and (C). The bottom image is the same blade but with LE probes of $D_{probe}/C_x = 0.03$ and $L_{probe}/C_x = 0.18$ mounted. The separation bubble is no longer apparent and the meandering cellular-structure of the surface streamlines at the trailing edge indicates the impact of the vortices shed from the LE probes. The additional disturbances introduced promote early transition in a similar manner to vortex generators (e.g. [20,21]), suppressing the separation bubble and hence reducing losses.

These observations demonstrate that there are competing mechanisms of separation bubble suppression and increasing bluff body drag. When LE probe diameters are small ($D_{probe}/C_x < 0.05$), the presence of the LE probes is advantageous at this Reynolds number because they suppress the separation bubble that would otherwise be present on an uninstrumented vane. However, for beyond a diameter ($D_{probe}/C_x > 0.05$), the bluff body drag penalty increasingly dominates.

Figure 21 plots surface static pressure profiles measured directly behind the central probe ($z/h = 0.5$) for the range of LE probe diameters tested ($0.02 < D_{probe}/C_x < 0.23$). In this figure it is clear that an increasing LE probe diameter leads to an increase in static pressure over the suction surface; with up to 90% length of the suction side and up to 40% length of the pressure side affected. This effect appears to be caused by the blockage induced by the probes, which tends to divert flow away from the instrumented blade. This phenomenon of flow redistribution around and within a blade passage in the presence of a blockage aligns with the observations of Lepicovsky [4] for a hub-mounted Kiel probe in a compressor rotor passage. Lepicovsky reported that the axial velocity within the instrumented passage was around 15% higher at the tip, with an overall axial velocity deficit of 4% of the rotor sector average for the entire passage, indicative of a significant diversion of the flow.

### 5.2 Length

Figure 22 shows the experimentally obtained mass averaged total pressure loss as a function of LE probe length spanning $0.08 < L_{probe}/C_x < 0.31$ for three constant diameters. It can be seen that probe length has very little effect on the measured total pressure loss coefficient for diameters of $D_{probe}/C_x = 0.03$ and 0.10, however, there is an appreciable decrease in loss with probe length for large diameter probes ($D_{probe}/C_x = 0.19$). Some insights into the behaviour may be gleamed from the surface static pressure distributions.

For the smallest probes, the only impact observed was the suppression of the separation bubble (figure 19). Comparing the static measurements directly behind the LE probe ($z/h = 0.5$) and between LE probes ($z/h = 0.583$), only minor differences are observed for $S/S_0 < 0.1$ which indicate that the spanwise variation induced by probes of $D_{probe}/C_x = 0.03$ is small.

For the larger diameter probes ($D_{probe}/C_x = 0.10$ and 0.19), two sets of static pressure distributions are plotted in figure 23, one measured directly in line with the central LE probe at blade midspan ($z/h = 0.5$), figures 23a and 23c, and one directly in-between two LE probes ($z/h = 0.583$), figures 23b and 23d. Pressure distributions for LE probe lengths of $L_{probe}/C_x = 0.08$, 0.18 and 0.31 are shown for each plot.

For probes of $D_{probe}/C_x = 0.10$ (figure 23a), the surface static pressures measured directly behind the central LE probe indicate a lower velocity than the design intent over the first 30% of the blade surface. Between LE probes (figure 23b), the deviation from the Mises intent is smaller. This comparison indicates that although the surface static $C_p$ is lower, pressure is higher overall due to the total blockage effect: the flow undergoes local spanwise redistribution so that the velocity between LE probes is approximately maintained. Although not shown in the current plot, the separation bubble that was observed previously (e.g. figure 19) does not appear for either of the measured distributions given a LE probe diameter of $D_{probe}/C_x = 0.10$, irrespective of length.

A more complex behaviour is observed in the pressure distributions for the larger diameter probe ($D_{probe}/C_x = 0.19$).

The measurements directly behind LE probes (figure 23c) show the general trend of lower $C_p$ compared to the design intent as noted above. On top of this effect, spikes in velocity are evident on the suction side at the LE ($S/S_0 < 0.1$), which increases as LE probe length decreases. These spikes indicate the effect of blockage due to separation, which becomes less severe for longer LE probes. Increasing the length of the probe body increases the available distance for the flow to reattach after separating from the probe LE. Therefore the flow arriving at the blade LE is attached to the probe body and the blockage at the LE is reduced. In contrast, the flow separation at the short LE probes will not reattach before the blade LE and therefore generates higher velocities and higher losses (figure 22). Between probes (figure 23d), a similar effect is observed but is less pronounced.

Based on the results, one may therefore conclude that the probe length has a small effect on blade aerodynamics and losses up to a certain probe aspect ratio ($L_{probe}/D_{probe}$). Hoerner [19] reports that the drag coefficients of cylindrical bodies in axial flow become invariant with cylinder aspect ratio above $L/D \approx 2$. The data in figure 22 is replotted as a function of LE probe aspect ratio ($L_{probe}/D_{probe}$) in figure 24. One can see that the total pressure loss coefficient is largely independent of LE probe aspect ratio for $L_{probe}/D_{probe} > 2$ in good agreement with Hoerner. Below this limiting aspect ratio, Hoerner shows that the location of bluff body separation becomes important and losses increase with the inverse of aspect ratio. However, in the current results there is no universal trend at low aspect ratio, with the $D_{probe}/C_x = 0.10$ cases showing little sensitivity even for $L_{probe}/D_{probe} < 1$, and the $D_{probe}/C_x = 0.19$ cases showing a strong dependence on aspect ratio for $L_{probe}/D_{probe} < 2$. This aspect ratio dependence may also be responsible for the rapid increase in parasitic losses for probe sizes between $0.19 \lesssim D_{probe}/C_x \lesssim 0.23$ (see figure 17 & 18). This effect could also indicate a significant interaction between adjacent probes. While the behaviour is more complex than a simple bluff body, for most applications the aspect ratio is above 2 and thus the effect of LE probe length would be expected to have little impact.

## 6 CONCLUSION

A complementary experimental and CFD study was conducted to assess the performance impact of leading edge probes mounted to the nozzle guide vane of a low pressure turbine. The vane and leading edge instruments were modeled in a low Mach number cascade and loss measurements were conducted with a calibrated five hole pressure probe. The following conclusions may be drawn;

1. A horseshoe vortex-like system forms at the leading edge probe and blade junction, while shroud bleed holes generate pairs of kidney vortices which advect downstream.
2. In general, the orientation of the shroud bleed holes has only a small impact on the induced parasitic losses. Compared to a realistic temperature Kiel, it was found that a solid cylinder of matching diameter and length produced 98% of the parasitic loss of a fully featured probe.
3. Parasitic loss is sensitive to leading edge probe incidence. LE probes of off-design incidence angles of up to 10 degrees were tested and caused variations of up to 30% in parasitic loss.

4. To a first order parasitic loss scales with probe frontal area and the behaviour is approximately equivalent to bluff body dynamics.
5. Probes can impact the boundary layer transition process and affect the loss. Small leading edge probes ($D_{probe}/C_x \approx 0.03$) suppressed a separation bubble that formed on the uninstrumented vane, reducing the profile loss by around 20%.
6. Parasitic loss is independent of probe length above a limiting probe aspect ratio ($L_{probe}/D_{probe} \approx 2$). Beyond a certain LE probe diameter, however, parasitic loss decreases with probe length.

With the general push towards smaller cores in aeroengines, it can be expected that non-dimensional probe sizes are likely to increase along with the parasitic losses induced. The findings of this paper have shown that, while losses scale to a first order with frontal area, a great deal of care is needed to accurately understand the losses induced and account for the impact on the engine performance. Further work is needed to examine and understand the more complex environment of engine realistic flows, in particular the sensitivity to inlet conditions, probe incidence, probe-to-probe and probe-to-endwall effects.

**Acknowledgements**

The authors would like to thank Rolls Royce plc. for funding, technical support and permission to publish this work, in particular Frederic Goenaga and David Lambie; thanks are also due to Mark Erland for his insights into probe design and operation. The insight and assistance of Howard Hodson and Chris Clark of the Whittle Laboratory are gratefully acknowledged. Funding was received through the SILOET II project.

**NOMENCLATURE**

| | |
|---|---|
| $\alpha$ | Blade incidence |
| $A_{probe}$ | LE probe frontal area |
| $A_{passage}$ | Cross sectional area of passage |
| $C_p$ | Surface static pressure coefficient: $(P_{01}-P)/(P_{01}-P_2)$ |
| $C_{p_{(TE)}}$ | Surface static pressure coefficient normalised by TE value: $(P_{01}-P)/(P_{01}-P_{TE})$ |
| $C_x$ | Axial chord |
| CFD | Computational fluid dynamics |
| $D_{5HP}$ | Five hole pressure probe head diameter |
| $D_{probe}$ | LE probe diameter |
| $\gamma$ | LE probe to blade incidence |
| $h$ | Blade span |
| $L_{probe}$ | LE probe length |
| $L_x$ | Streamwise integral length-scale |
| LE | Leading edge |

| | |
|---|---|
| $M_2$ | Exit Mach number |
| $\nu$ | Kinematic viscosity |
| NGV | Nozzle guide vane |
| $P$ | Surface static pressure |
| $P_{01}$ | Inlet total pressure |
| $P_1$ | Inlet static pressure |
| $P_{02}$ | Exit total pressure |
| $P_2$ | Exit static pressure |
| $R_f$ | Recovery factor:$(T_m - T_s)/(T_t - T_s)$ |
| PS | Pressure side |
| RANS | Reynolds averaged Navier-Stokes |
| $Re$ | Reynolds number |
| $Re_{5HP}$ | Five hole pressure probe Reynolds number |
| $s$ | Blade pitch |
| $S$ | Blade surface length |
| $S_0$ | Total blade surface length |
| SS | Suction side |
| $T_m$ | Measured temperature |
| $T_s$ | Static temperature |
| $T_t$ | True stagnation temperature |
| TE | Trailing edge |
| $Tu$ | Freestream turbulence intensity |
| $U_\infty$ | Freestream velocity |
| $x$ | Axial/Streamwise direction |
| $Y_p$ | Total pressure loss coefficient |
| $z$ | Spanwise/Radial direction |

**References**


[1] Kiel, G., 1935. Total-head meter with small sensitivity to yaw. Tech. rep., NACA, August. Technical Note 775.

[2] Russell, W. R., Gracey, W., Letko, W., and Fournier, P. G., 1951. Wind-tunnel investigation of six shielded total-pressure tubes at high angles of attack subsonic speeds. Tech. rep., NACA, November. Technical Note 2530.

[3] Gracey, W., 1956. Wind-tunnel investigation of a number of total-pressure tubes at high angles of attack subsonic, transonic and supersonic speeds. Tech. rep., NACA, May. Technical Note 3641.

[4] Lepicovsky, J., 2008. Effects of a rotating aerodynamic probe on the flow field of a compressor rotor. Tech. rep., NASA, June. NASA/CR–2008-215215.

[5] Stieger, R. D., and Hodson, H. P., 2004. "The transition mechanism of highly loaded low pressure turbine blades". *Journal of Turbomachinery,* **126**, pp. 536–543.

[6] Drela, M., 1985. "Two-dimensional transonic aerodynamic design and analysis using the Euler equations". PhD thesis, Massachusetts Institute of Technology.

[7] Youngren, H., and Drela, M., 1991. "Viscous/inviscid method for preliminary design of transonic cascades". *AIAA Paper,* **91**, p. 2364.

[8] Roach, P. E., 1987. "The generation of nearly isotropic turbulence by means of grids". *Heat and Fluid Flow,* **8**(2), pp. 82–92.

[9] Moinier, P., and Giles, M. B., 1998. "Preconditioned Euler and Navier-Stokes calculations on unstructured meshes". $6^{th}$ *ICFD Conference on Numerical Methodsfor Fluid Dynamics*.

[10] Dargahi, B., 1989. "The turbulent flow field around a circular cylinder". *Experiments in Fluids,* **8**, pp. 1–12.

[11] Williamson, C. H. K., 1996. "Vortex dynamics in the cylinder wake". *Ann. Rev. Fluid Mech.,* **28**, pp. 477–539.

[12] Kirkil, G., and Constantinescu, G., 2015. "Effect of cylinder Reynolds number on the turbulent horseshoe vortex system and newar wake of a surface-mounted circular cylinder". *Physics of Fluids,* **27**(7), p. 075102.

[13] Hunt, J. C. R., Wray, A. A., and Moin, P., 1988. Eddies, stream and convergence zones in turbulent flows. Tech. rep., Stanford. Center for Turbulence Research Report CTR-S88.

[14] Broadwell, J. E., and Breidenthal, R. E., 1984. "Structure and mixing of a transverse jet in incompressible flow". *Journal of Fluid Mechanics,* **148**, pp. 405–412.

[15] Fric, T. F., and Roshko, A., 1994. "Vortical structure in the wake of a transverse jet". *Journal of Fluid Mechanics,* **279**, pp. 1–47.

[16] Kelso, R. M., Lim, T. T., and Perry, A. E., 1996. "A experimental study of round jets in cross-flow". *Journal of Fluid Mechanics,* **306**, pp. 111–144.

[17] Haven, B. A., and Kurosaka, M., 1997. "Kidney and anti-kidney vortices in crossflow jets". *Journal of Fluid Mechanics,* **352**, pp. 27–64.

[18] Bunker, R. S., 2005. "A review of shaped hole turbine film cooling technology". *Journal of hear transfer,* **127**, pp. 441–453.

[19] Hoerner, F. S., 1965. *Fluid-dynamic drag: theoretical, experimental and statistical information.* Hoerner Fluid Dynamics, U.S.A.

[20] Schubauer, G. B., and Spangenberg, W. G., 1960. "Forced mixing in boundary layers". *Journal of Fluid Mechanics,* **8**, pp. 10–32.

[21] Westphal, R. V., Pauley, W. R., and Eaton, J. K., 1987. Interaction between a vortex and a turbulent boundary layer. Part 1: Mean flow evolution and turbulence properties. Tech. rep., NASA, January. TM-88361.

## TABLES

| BLADE PARAMETERS | |
|---|---|
| Chord($C$)[m] | 0.233 |
| Axial Chord($C_x$)[m] | 0.193 |
| Pitch($s$)[m] | 0.169 |
| Span($h$)[m] | 0.375 |
| Inlet flow angle($\alpha_1$)[°] | -15.7 |
| Exit flow angle($\alpha_2$)[°] | -53.9 |
| Zweifel coefficient($Z_w$) | 0.689 |
| Diffusion factor($D_v$) | 0.230 |
| $Re$ | 330000 |
| TURBULENCE GRID PARAMETERS | |
| Bar size[m] | 0.006 |
| Porosity | 0.5 |
| Distance to LE[m] | 0.64 |
| $Tu$% | 4 |
| $L_x$[m] | 0.012 |

Table 1: CASCADE SPECIFICATIONS

| CASE | EXPERIMENT | $Y_p$ | Parasitic loss ($Y_p - Y_{p_{(CLEAN)}}$) | $Y_p - Y_{p_{(TEMP.\ KIEL)}}$ |
|---|---|---|---|---|
| 0 | Clean | 0.0166 | 0 | -0.0110 |
| 1 | Shroud bleed holes 0° | 0.0276 | 0.0110 | 0 |
| 2 | Shroud bleed holes 45° | 0.0248 | 0.0082 | -0.0028 |
| 3 | Shroud bleed holes 90° | 0.0266 | 0.0100 | -0.0010 |
| 4 | Shroud bleed holes covered | 0.0268 | 0.0102 | -0.0008 |
| 5 | Cylinders | 0.0271 | 0.0105 | -0.0005 |

Table 2: TOTAL PRESSURE LOSS COEFFICIENTS FOR TEST CASES EXAMINING THE EFFECT OF SHROUD BLEED HOLES.

**FIGURES**

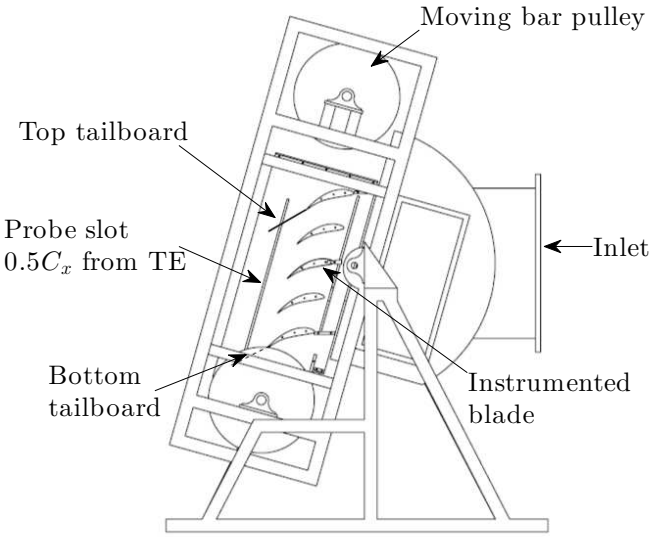


Fig. 1: SKETCH OF CASCADE WITH INSTRUMENTED BLADE.

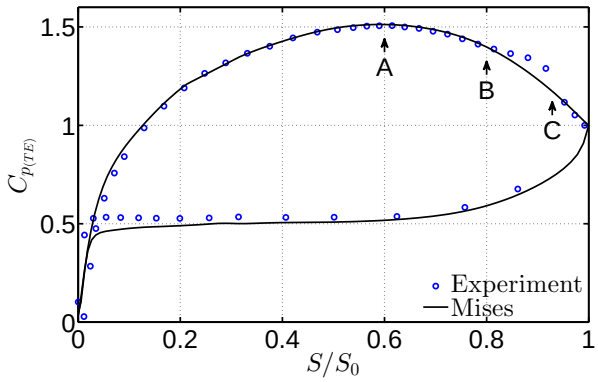


Fig. 2: MEASURED BLADE STATIC PRESSURE DISTRIBUTION FOR UNINSTRUMENTED VANE (BLUE) AND MISES TARGET DISTRIBUTION (BLACK).

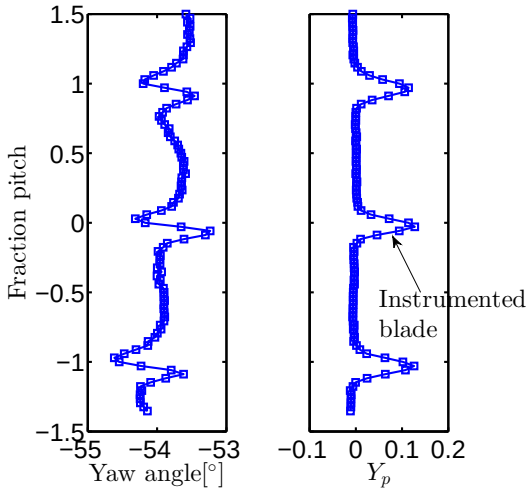


Fig. 3: PLOTS OF YAW ANGLE AND $Y_p$ TAKEN AT CASCADE MIDSPAN FOR PASSAGES ADJACENT TO INSTRUMENTED BLADE.

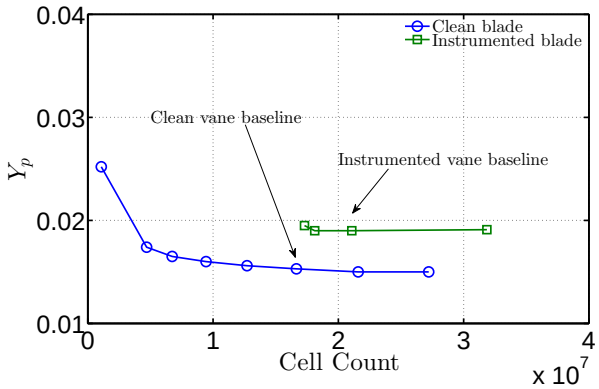


Fig. 4: MASS AVERAGED $Y_P$ AS A FUNCTION OF CELL COUNT SHOWING BASELINE REFINEMENT LEVELS FOR A CLEAN VANE AND INSTRUMENTED VANE.

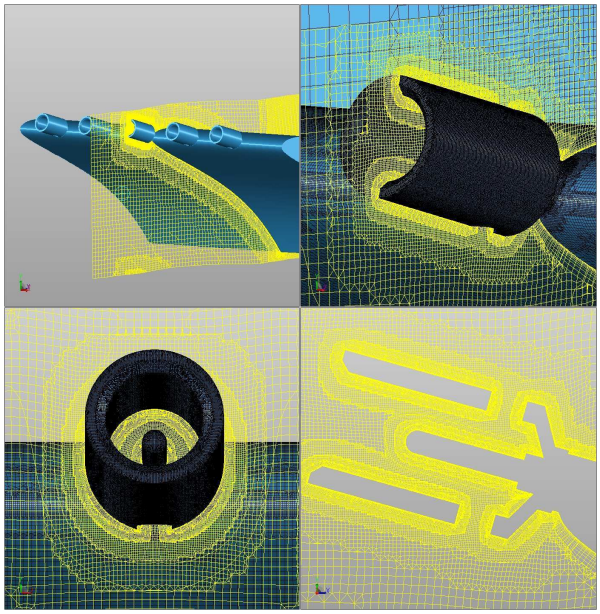

Fig. 5: MESH OF INSTRUMENTED VANE AND MESH DETAILS OF REALISTIC TEMPERATURE PROBE.

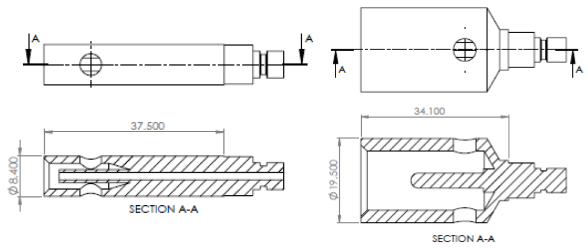


Fig. 6: SKETCH OF REALISTIC PROBE MODELS. LEFT: PRESSURE PROBE, RIGHT: TEMPERATURE PROBE.

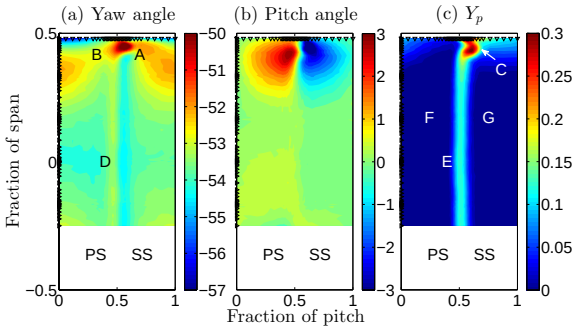


Fig. 7: LEFT-TO-RIGHT: CONTOURS OF YAW ANGLE, PITCH ANGLE AND $Y_p$ MEASURED WITH A 5-HOLE PROBE AT CASCADE EXIT FOR UNINSTRUMENTED VANE.

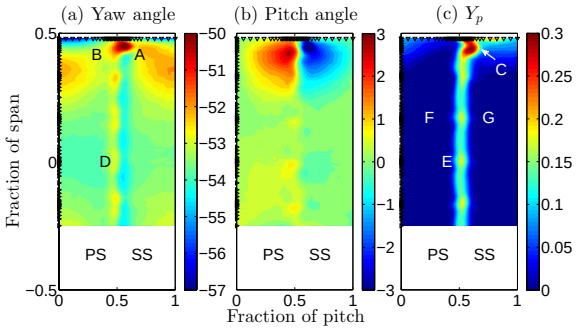


Fig. 8: LEFT-TO-RIGHT: CONTOURS OF YAW ANGLE, PITCH ANGLE AND $Y_p$ MEASURED WITH A 5-HOLE PROBE AT CASCADE EXIT FOR REALISTIC PRESSURE PROBES.

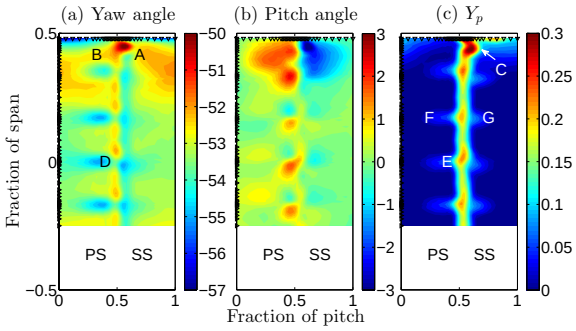


Fig. 9: LEFT-TO-RIGHT: CONTOURS OF YAW ANGLE, PITCH ANGLE AND $Y_p$ MEASURED WITH A 5-HOLE PROBE AT CASCADE EXIT FOR REALISTIC TEMPERATURE PROBES.

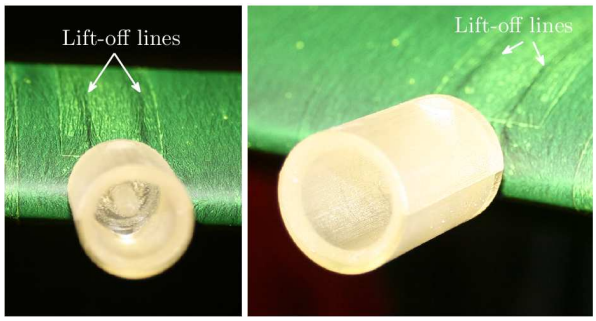


Fig. 10: FLOW VISUALISATION FOR THE REALISTIC TEMPERATURE PROBE.

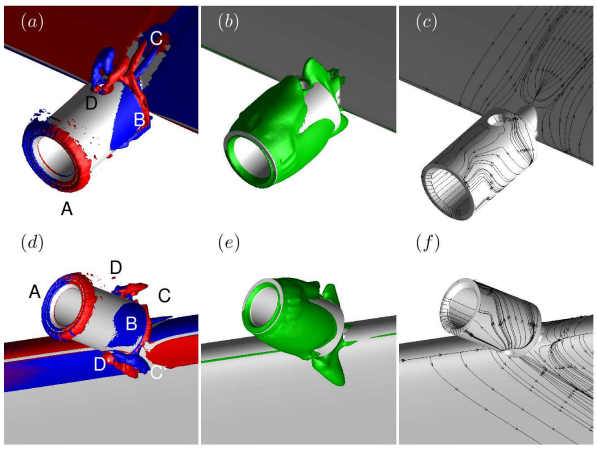


Fig. 11: ISOSURFACES OF Q COLORED BY VORTICITY (a) AND (d), VIEWING THE LE PROBE FROM THE SUCTION SIDE AND PRESSURE SIDE, RESPECTIVELY. CORRESPONDING ISOSURFACES OF NEGATIVE AXIAL VELOCITY (b) AND (e) AND CORRESPONDING SURFACE STREAMLINES (c) AND (f).

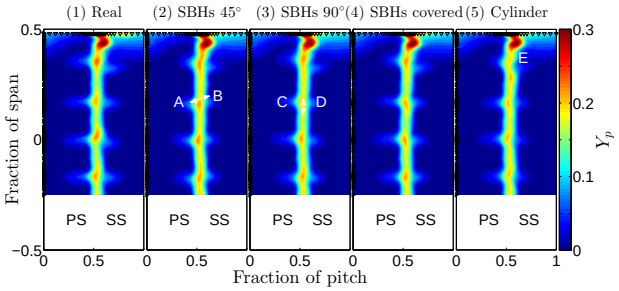


Fig. 12: CONTOURS OF $Y_p$ FOR EACH TEST CASE. FROM LEFT-TO-RIGHT:(1) REAL TEMPERATURE KIELS, (2) SHROUD BLEED HOLES AT 45 DEGREES, (3) SHROUD BLEED HOLES AT 90 DEGREES, (4) SHROUD BLEED HOLES COVERED AND (5) SOLID CYLINDERS.

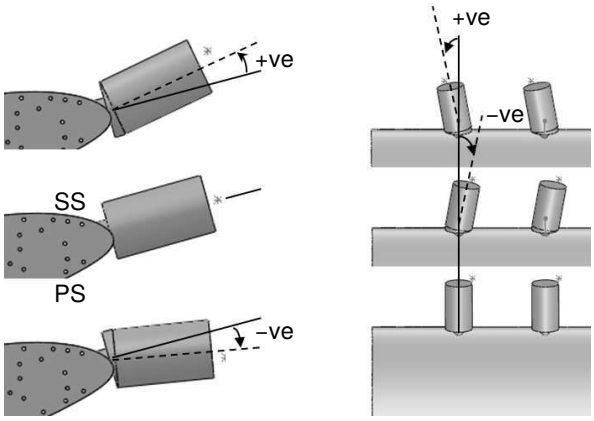


Fig. 13: SCHEMATIC OF PROBE INCIDENCE. LEFT: LE PROBE YAW ANGLE RELATIVE TO DESIGN. RIGHT: LE PROBE PITCH ANGLE RELATIVE TO DESIGN.

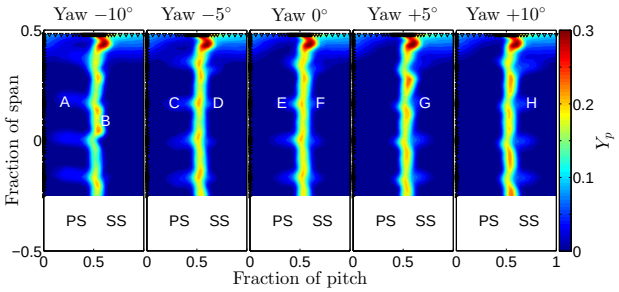


Fig. 14: CONTOURS OF $Y_p$ FOR LE PROBE YAW ANGLES AS INDICATED

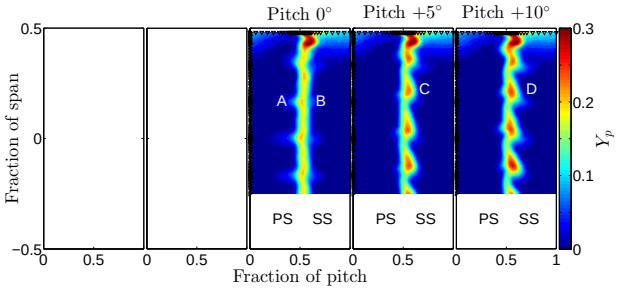


Fig. 15: CONTOURS OF $Y_p$ FOR LE PROBE PITCH ANGLES AS INDICATED

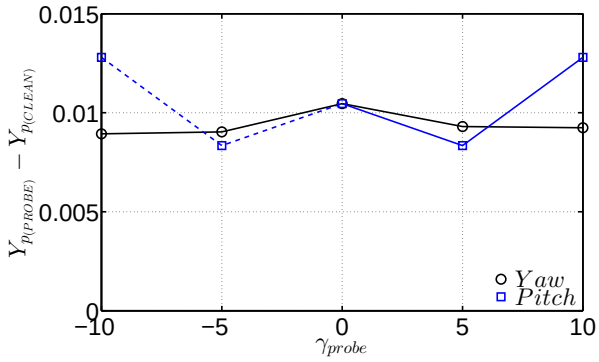


Fig. 16: MASS AVERAGED $Y_p$ AS A FUNCTION OF LE PROBE INCIDENCE RELATIVE TO DESIGN INLET.

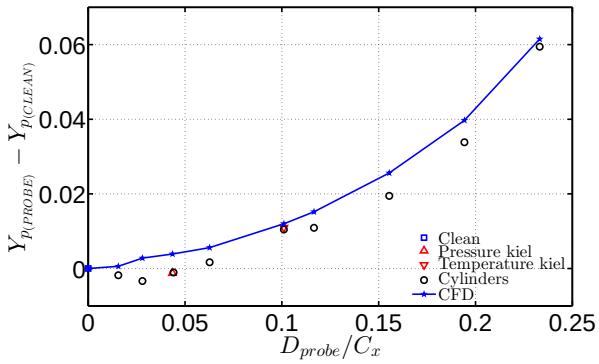


Fig. 17: MASS AVERAGED $Y_p$ AS A FUNCTION OF LE PROBE DIAMETER. CONSTANT PROBE LENGTH $L_{probe}/C_x = 0.18$.

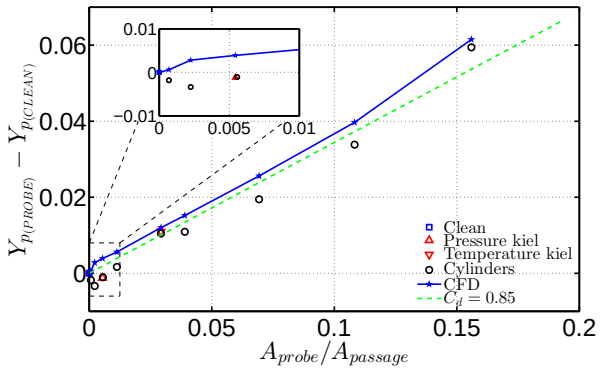


Fig. 18: MASS AVERAGED $Y_p$ AS A FUNCTION OF PROBE FRONTAL AREA-TO-PASSAGE AREA. CONSTANT PROBE LENGTH $L_{probe}/C_x = 0.18$.

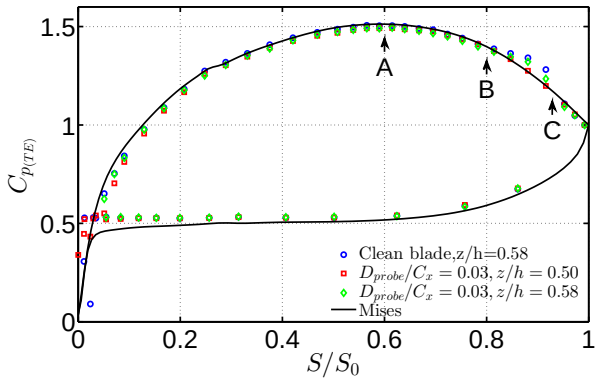


Fig. 19: MEASURED BLADE STATIC PRESSURE DISTRIBUTION FOR UNINSTRUMENTED VANE (BLUE); VANE WITH $D_{probe}/C_x = 0.03$ PROBES MOUNTED (RED AND GREEN) AND MISES TARGET DISTRIBUTION (BLACK).

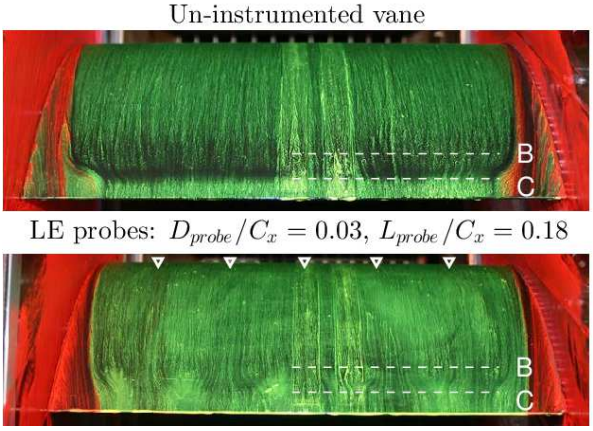


Fig. 20: FLOW VISUALISATION PHOTOS OF SUCTION SIDE BLADE SURFACE. TOP: UNINSTRUMENTED BLADE WITH SEPARATED REGION BETWEEN (B) AND (C). BOTTOM: LE PROBES OF $D_{probe}/C_x = 0.03$ AND $L_{probe}/C_x = 0.18$ MOUNTED. LE PROBE LOCATIONS INDICATED BY WHITE TRIANGLES IN IMAGE. NOTE SUPPRESSION OF SEPARATION REGION IN BOTTOM PHOTO.

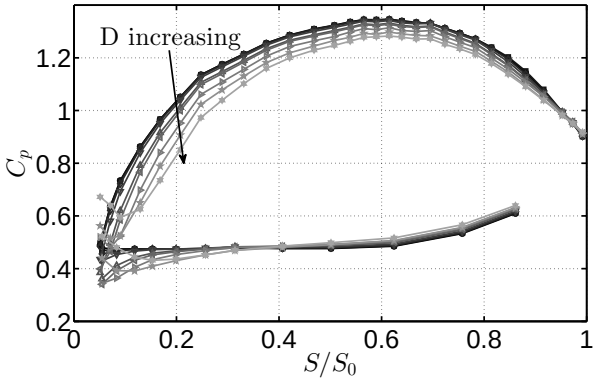


Fig. 21: BLADE STATIC PRESSURE DISTRIBUTION FOR INCREASING LEADING EDGE PROBE DIAMETERS AND CONSTANT LENGTH $L_{probe}/C_x = 0.18$.

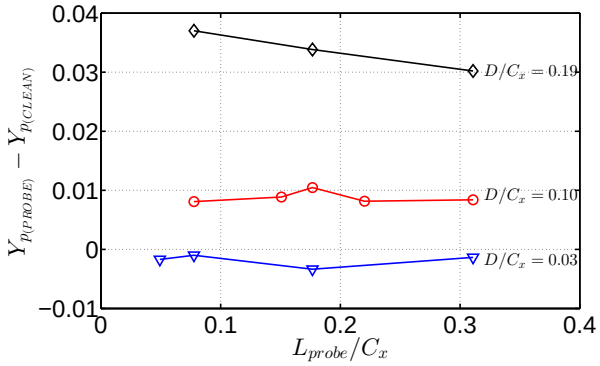


Fig. 22: MASS AVERAGED $Y_p$ AS A FUNCTION OF LE PROBE LENGTH. INCREASING DIAMETERS AS LABELED.

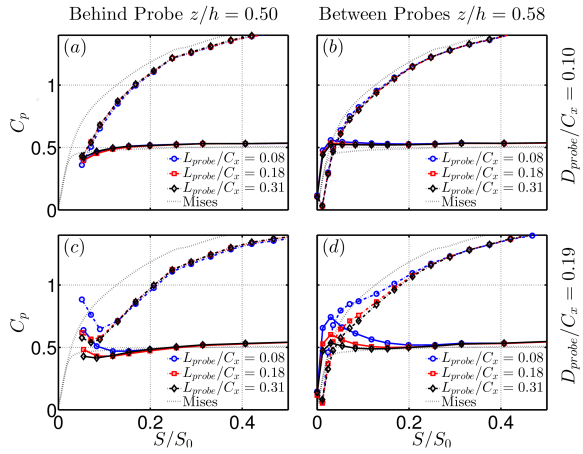


Fig. 23: BLADE STATIC PRESSURE DISTRIBUTION MEASURED DIRECTLY BEHIND LE PROBES (LEFT) AND BETWEEN LE PROBES (RIGHT), FOR INCREASING LENGTH ($0.08 < L_{probe}/C_x < 0.31$) AT CONSTANT DIAMETERS: $D_{probe}/C_x = 0.10$ (TOP) AND 0.19 (BOTTOM). MISES DESIGN INTENT PLOTTED FOR REFERENCE.

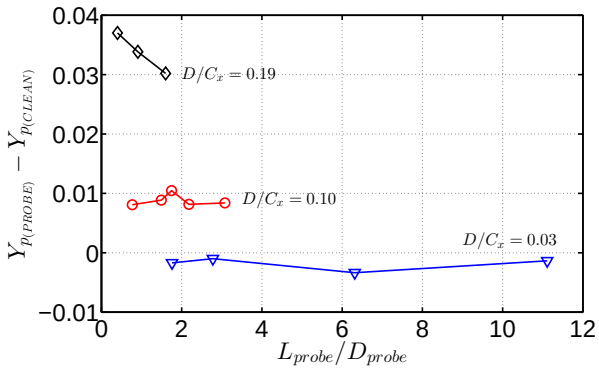


Fig. 24: MASS AVERAGED $Y_p$ AS FUNCTION OF LE PROBE LENGTH ASPECT RATIO. PROBE DIAMETERS AS LABELED.